The 20th International Conference on
Transport and Sedimentation of Solid Particles
26–29th September 2023, Wroclaw, Poland

ISSN 0867-7964 ISBN 978-83-7717-392-3

# EXPERIMENTAL AND NUMERICAL ANALYSIS OF IRON ORE SLURRY FLOW THROUGH PIPELINE AT VERY HIGH CONCENTRATION

**Stuti Mishra and Deo Raj Kaushal**

**DOI: 10.30825/4.14-18.2023**

*Civil Engineering Department, IIT Delhi, INDIA*
*e-mail: kaushal@civil.iitd.ac.in*

ABSTRACT: A slurry pipeline is a specially designed pipeline used to transport the mining tailings and waste of ores like iron or coal over long distances. A commercially tested solution for the transport of iron ore slurry over the farthest distances in a pipeline includes various parametric checks. For the slurry to move, consuming optimal power in the pipe while maintaining the required velocity, it is important to keep some parameters within the desired limits, the most important of which is the pressure drop in the slurry pipeline. Pilot plant loop tests were conducted with iron ore slurry at high concentration (72% by weight or 32.7% by volume). The flow velocities were set in the range of 1.5 m/s to 4 m/s and the pressure drop per unit length was measured for each flow velocity using the U-tube differential manometer installed in the setup. The pressure drop values were also calculated using standard equations available in the literature and deviations up to 221% from experimental values were observed. Alternatively, a CFD model was developed using Ansys Fluent© and validated using the experimental results. This was a first attempt to predict such flows, and further tests are needed to confirm the initial results.

KEY WORDS: Slurry pipeline, CFD (Computational Fluid Dynamics), Ansys Fluent©.

## NOTATION

| | |
|---|---|
| $\tau$ | Shear stress (Pa) |
| $\tau_o$ | Yield stress (Pa) |
| $\mu_B$ | Absolute viscosity of Bingham plastic (Pa-s) |
| $\dot{\gamma}$ | Shear rate (1/s) |
| $\sigma$ | Tensile stress (Pa) |
| $\rho$ | Density (Kg/m$^3$) |
| D | Diameter of pipeline (m) |
| V | Velocity (m/s) |

## 1. INTRODUCTION

Fine iron ore slurry with a high solids concentration can be transported via pipeline from the mine to the location where it will be used, with both technological and financial ramifications. Transporting iron ore slurry with a high solids concentration could be a creative way to lower the amount of water needed to produce each ton of ore slurry. For a long time, several businesses and power plants have been using slurry transportation. Many organizations prefer slurry transport over lengthy pipelines because it provides a number of advantages, including no contamination, no traffic, low power usage, and constant delivery, among others. Industries move solids, including rock, coal ash, iron ore, copper, zinc tailing, and concrete material, as slurry with water to the best transportation location.

Despite significant research, the prediction of pressure drop in slurry pipelines is still a problematic issue for design engineers. The design of slurry pipelines depends on the experimental and empirical correlations obtained. Although the empirical formula and relations have been developed with high precision, but when the local solid concentration is high, the error in the predictions starts increasing. Considering this, the development of computational models becomes most useful, which allows a prior estimation of pressure drop, velocity profile and solid concentration over the entire pipeline's length and cross-section. Solving problems involving fluid flow, heat and mass transfer, chemical processes, and other phenomena has made CFD a potent tool in recent years.

There have been very limited studies on the experimental and numerical studies of high concentration iron ore slurry due to several complexities, such as the high specific gravity of the material, and the high concentration leading to difficulty in pressure drop measurement, among which the most common is choking of the pipeline. Mishra et al. (2023) did a CFD analysis of the pressure variation inside the iron ore slurry pipelines. Their work focused on the determination of pressure drop at the ends of a pipeline, concluding that higher values of radius of curvature and lower values of inlet velocity are the most optimal flow conditions for the slurry in a pipeline. Kumar et al. (2019) generated a detailed dataset of experimental results from the pilot plant test using a 4 inches (101 mm mean diameter) slurry pipeline for iron ore slurries. Furthermore, the results were validated using a CFD based model. Their study showed a thorough investigation of the slurry over a wide concentration range, up to 31% by volume. Avksentiev et al. (2017) developed a methodology to calculate the head losses and hydraulic resistance coefficient on the basis of the rheological behavior of iron ore slurry for the design purposes of the pipelines. Their work focused on the correlation of various factors, such as initial shear stress, and dynamic viscosity, for the development of the Bingham-Shvedov model. Yang et al. (2020) studied iron ore fine tailing for its shear dependent yield stress behavior using a two-step flocculation process. Primary and secondary phases in flocculation helped in predicting the shear resistance of the iron ore slurry.

Studies on different materials have been done for pressure drop analysis. Developing an accurate and precise computational model is very important to predict the future pressure losses and concentration profiles in a pipeline. Nagar et al. (2021) measured the pressure drop and concentration profiles caused by 25 mm fly ash particles combined with water to form a solid-liquid slurry in a 50 mm conduit, CFD simulations were performed. To study the flow patterns of solid-liquid flow, pressure drop and concentration profiles

were predicted and assessed in relation to actual flow parameters. The design of a slurry pipeline will benefit from this study as well. Messa et al. (2021) did a thorough review of the CFD models for solid-liquid flows in a pipeline, focusing on the challenges one can encounter during the CFD approach and the uncertainty of the CFD models for their predictive capacity. Kumar N. et al., (2019) did a CFD analysis for fly ash slurry of 21μm in a 50 mm pipeline using a two phase Eulerian-Eulerian model. They also measured the concentration and velocity profiles efficiently using Ansys software. For particle laden flow, CFD-DEM models appeared to be a suitable approach, and the eulerian-eulerian model was found to result in the best fit to simulate slurry flow in pipelines. Since the rheological characteristics of iron ore slurry play a pivotal role in predicting the flow behavior of slurry inside the pipeline, Das et al., (2020) conducted an important study on the stabilization of iron ore slurry for its economic transportation. Their surface chemistry and characteristics are broadly studied to see the changes in iron ore slurry during its transportation. Prakash et al., (2019) carried out a detailed comparative analysis of pressure drop estimation in a horizontal and vertical pipeline, and glass bead slurry was chosen as a secondary phase. The results of velocity contours, solid concentration profiles and pressure drops were predicted.

In view of the experimental and CFD based modelling available in literature for iron ore slurry concentrations only up to 31% by volume, the present study is carried out to study flow behavior and its CFD based modelling at a higher concentration of 32.7% by volume (72% by weight).

## 2. METHODOLOGY

The goal of this investigation was to find the most accurate method to validate the experimental results of pressure drop. Iron ore fines were collected from a mining site in Chattisgarh, India. A particle size distribution test was done, which comprised sieve analysis (for particles >75 μm) and hydrometer test (for particles <75μm) after which the d50 of the particles was found to be 55 μm. The specific gravity of iron ore measured using the gravitational method was 5.3. The maximum packing concentration was measured at 36% by volume.

### 2.1. EXPERIMENTAL METHOD

Fresh slurry was made with a 72% w/w iron ore sample and poured into the pipe-loop setup, which consists of a 2-inch (50.8mm mean diameter) pipe. Pressure drop was measured using a U-tube manometer with pressure points placed at a distance greater than 50D from the inlet to get the full flow development. The setup was run at different velocities which were measured using an EMF (electro-magnetic flowmeter) where the speed of the slurry pump was connected to a controller. Pressure drop was measured at each velocity and converted into the desired unit (kPa/m).

## 2.2. THEORETICAL METHOD

For the determination of the pressure drop in a pipeline, it is important to know the properties of the slurry and the type of flow. The rheological properties of the flow were calculated using the ANTONpar RheoLab QC. The shear rate was varied from 300 to 30 rpm, and shear stress was found out for the provided shear rate. With the help of the obtained shear stress - shear rate graph, the best fit was found to be for Bingham plastic, since the curve followed a straight line with a positive intercept on the y-axis. The standard equation is given by equation (1).

$$\tau = \tau_0 + \mu_B \gamma \tag{1}$$

The absolute viscosity and yield stress were calculated using the slope and intercept of the bingham shear stress-shear rate curve and further used to calculate the Hedstrom number and Bingham Reynolds number for the flow using equations (4) and (2), respectively.

Two standard methods were used to calculate the pressure drop for iron ore slurry in a pipeline.

For the Chhabra and Richardson (2011) method, the Hedstrom number and Bingham's Reynolds number are used to determine the friction factor from Figure (1), which is used to calculate the pressure drop from equation (3).

Bingham Reynolds number $Re_B = \frac{\rho V D}{\mu_B}$ (2)

Friction factor, $f = \frac{\tau_w}{(\frac{1}{2})\rho V^2} = \frac{D(-\frac{\Delta p}{L})}{2\rho V^2}$ (3)

Hedstrom number, $He = \frac{\rho D^2 {\tau_0}^B}{\mu_B^2}$ (4)

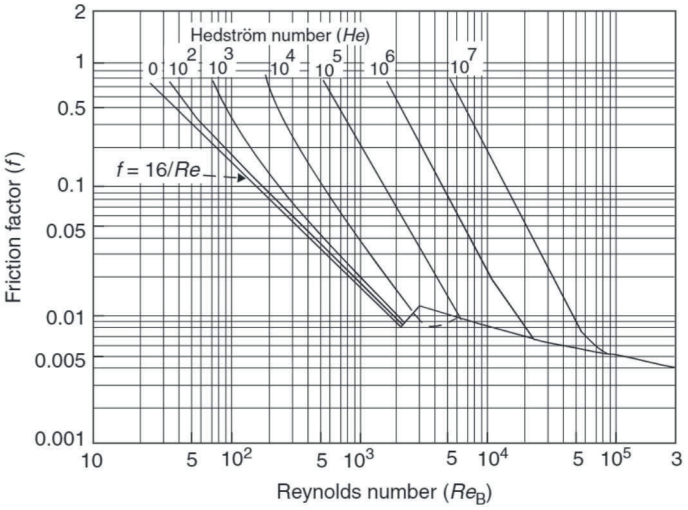


Figure 1 Graph representing friction factor as a function of Reynolds and Hedstrom numbers [2]

For the Darby and Melson (1981) method, the Hedstrom number and Bingham Reynolds number is calculated as above in equations (2) and (4). To get a single explicit friction factor equation valid for all the flow regimes, they have developed the following equation.

$$f = [f_L^m + f_T^m]^{\frac{1}{m}} \tag{5}$$

where, $m = 1.7 + \frac{40000}{Re_B}$

Friction factor for laminar pipe flow, $f_L = \frac{64}{Re_B}[1 + \frac{He}{6Re_B} - \frac{64}{3}\left(\frac{He^4}{f_L^3 Re_B^7}\right)]$ (6)

Friction factor for turbulent flow, $f_T = 10^a Re^{-0.193}$ (7)

where $a = -1.47[1 + 0.146e^{-2.9*10^{-5}He}]$

## 2.3 NUMERICAL METHOD

The flow behaviour of a fluid-solid mixture is described by FLUENT using a multi-fluid granular model. By drawing an analogy between the random particle motion brought on by particle-particle collisions, the solid-phase stresses are obtained. Ansys Fluent 2021 was used. Here, the Eulerian-Eulerian two-fluid model is used, in which the solid and liquid phases are both considered to be in continuum. This method allows for the finding of distinct flow field solutions because the continuity and momentum equations are solved for each phase. Among the multiphase models, the Eulerian model is the most intricate and computationally demanding. For each phase, it resolves a group of "n" number of momentum and continuity equations. The pressure and interphase exchange coefficients are coupled to each other. Application of the kinetic theory yields the properties for granular flows.

Different forces are acting on a single particle of fluid [Kaushal et al. 2012]:

1. Static pressure gradient, $\nabla P$.
2. Solid pressure gradient or the inertial force due to particle interactions, $\nabla P_s$.
3. Drag force caused by the velocity differences between two phases, $K_{sf}(\vec{v}_s - \vec{v}_f)$, where, $K_{sf}$ is the inter-phase drag coefficient, $\vec{v}_s$ and $\vec{v}_f$ are the velocity of solid and fluid phase.
4. Viscous forces, $\nabla \cdot \bar{\bar{\tau}}_f$, where, $\bar{\bar{\tau}}_f$ is the stress tensor for fluid.
5. Body forces, $\rho \vec{g}$ where, $\rho$ is the density and g is acceleration due to gravity.
6. Virtual mass force, $C_{vm}\alpha_s\rho_f(\vec{v}_f \cdot \nabla\vec{v}_f - \vec{v}_s \cdot \nabla\vec{v}_s)$, where, $C_{vm}$ is the coefficient of virtual mass force.
7. Lift force, where, $C_L\alpha_s\rho_f(\vec{v}_f - \vec{v}_s) \times (\nabla \times \vec{v}_f)$ where, $C_L$ is the lift coefficient.

### 2.3.1 Governing equations

#### 2.3.1.1 Continuity equation.

The solution of a continuity equation for the volume fraction of one (or more) of the phases allows for the tracking of the interface(s) between the phases is given as;

$$\nabla \cdot (\alpha_t \rho_t \vec{v}_t) = 0 \tag{8}$$

where, t is either solid(s) or fluid(f).

#### 2.3.1.2 Momentum equations.

For fluid phase:

$$\nabla \cdot (\alpha_f \rho_f \vec{v}_f \vec{v}_f) = -\alpha_f \nabla P + \nabla \cdot \bar{\bar{\tau}}_f + \alpha_f \rho_f \vec{g} + K_{sf}(\vec{v}_s - \vec{v}_f) + C_{vm}\alpha_f \rho_f (\vec{v}_s \cdot \nabla \vec{v}_s - \vec{v}_f \cdot \nabla \vec{v}_f) + C_L \alpha_s \rho_f (\vec{v}_f - \vec{v}_s) \times (\nabla \times \vec{v}_f) \tag{9}$$

For solid phase:

$$\nabla \cdot (\alpha_s \rho_s \vec{v}_s \vec{v}_s) = -\alpha_s \nabla P - \nabla P_s + \nabla \cdot \bar{\bar{\tau}}_s + \alpha_s \rho_f \vec{g} + K_{fs}(\vec{v}_f - \vec{v}_s) + C_{vm}\alpha_s \rho_f (\vec{v}_f \cdot \nabla \vec{v}_f - \vec{v}_s \cdot \nabla \vec{v}_s) + C_L \alpha_s \rho_f (\vec{v}_s - \vec{v}_f) \times (\nabla \times \vec{v}_f) \tag{10}$$

where, $\bar{\bar{\tau}}_f$ and $\bar{\bar{\tau}}_s$ are the stress tensors for fluid and solid, which are expressed as;

$$\bar{\bar{\tau}}_f = \alpha_f \mu_f (\nabla \vec{v}_f + \nabla \vec{v}_f^{\,tr}) \tag{11}$$

and

$$\bar{\bar{\tau}}_s = \alpha_s \mu_s (\nabla \vec{v}_s + \nabla \vec{v}_s^{\,tr}) + \alpha_s (\lambda_s - \tfrac{2}{3}\mu_s) \nabla \cdot \vec{v}_s \bar{\bar{I}} \tag{12}$$

where the superscript 'tr' over velocity vector indicating transpose. $\bar{\bar{I}}$ is the identity tensor. $\lambda_s$ is the bulk viscosity of the solids as given by:

$$\lambda_s = \tfrac{4}{3}\alpha_s \rho_s d_s g_{0,ss}(1 + e_{ss})(\tfrac{\Theta_s}{\pi})^{\frac{1}{2}} \tag{13}$$

where $d_s$ is the particle diameter as 55µm. $g_{0,ss}$ is the radial distribution function, which is interpreted as the probability of particle touching another particle is given as:

$$g_{0,ss} = \left[1 - \left(\frac{\alpha_s}{\alpha_{s,max}}\right)^{\frac{1}{3}}\right]^{-1} \tag{14}$$

$\alpha_{s,max}$ is the static-settled concentration measured experimentally as 0.36 for the iron ore used in this work. $\Theta_s$ is the granular temperature, which is proportional to the kinetic energy of the fluctuating particle motion. $e_{ss}$ is the restitution coefficient, taken as 0.9 for iron ore particles. $\mu_f$ is the shear viscosity of fluid, $\mu_s$ is the shear viscosity of solids defined as

$$\mu_s = \mu_{s,col} + \mu_{s,kin} + \mu_{s,fr} \tag{15}$$

where, $\mu_{s,col}$ , $\mu_{s,fr}$ and $\mu_{s,kin}$ are collisional, frictional and kinetic viscosity. They are calculated using the following expressions:

$$\mu_{s,col} = \frac{4}{3}\alpha_s \rho_s d_s g_{0,ss}(1+e_{ss})\left(\frac{\Theta_s}{\pi}\right)^{\frac{1}{2}} \tag{16}$$

$$\mu_{s,fr} = \frac{P_s sin\phi}{2\sqrt{I_{2D}}} \tag{17}$$

and

$$\mu_{s,kin} = \frac{\alpha_s d_s \rho_s \sqrt{\Theta_s \pi}}{6(3-e_{ss})}\left[1+\frac{2}{5}(1+e_{ss})(3e_{ss}-1)\alpha_s g_{0,ss}\right] \tag{18}$$

$I_{2D}$ is the second invariant of the deviatoric strain rate tensor for solid phase. $P_s$ is the solid pressure as given by:

$$P_s = \alpha_s \rho_s \Theta_s + 2\rho_s(1+e_{ss})\alpha_s{}^2 g_{0,ss}\Theta_s \tag{19}$$

$\phi$ is is the internal friction angle taken as 30° in the present computations. $K_{sf}(=K_{fs})$ is the interphasial momentum exchange coefficient given by

$$K_{sf} = K_{fs} = \frac{3}{4}\frac{\alpha_s \alpha_f \rho_f}{V_{r,s}^2 d_s} C_D\left(\frac{Re_s}{V_{r,s}}\right)|\vec{v}_s - \vec{v}_f| \tag{20}$$

$$\text{Drag coefficient, } C_D = \left[0.63 + 4.8\left(\frac{Re_s}{V_{r,s}}\right)^{-\frac{1}{2}}\right]^2 \tag{21}$$

$Re_s$ is the relative Reynolds number between phases 'f' and 's' given by:

$$Re_s = \frac{\rho_s d_s |\vec{v}_s - \vec{v}_f|}{\mu_f} \tag{22}$$

$V_{r,s}$ is the terminal velocity correlation for solid phase given by:

$$V_{r,s} = 0.5\left(A - 0.06Re + \sqrt{(Re_s)^2 + 0.12Re_s(2B-A) + A^2}\right) \tag{23}$$

with

$$A=\alpha_f^{4.14}; B = \alpha_f^{1.28} \text{ for } \alpha_f \leq 0.85, \tag{24}$$

and

$$A=\alpha_f^{4.14}; B = \alpha_f^{2.65} \text{ for } \alpha_f > 0.85 \tag{25}$$

**2.3.2 Turbulence closure for the fluid phase**

Using the standard k-$\varepsilon$ model, predictions for turbulent quantities for the fluid phase are made, supplemented by additional terms that account for the transport of turbulent momentum transfer across interfaces.

The Reynolds stress tensor for the fluid phase 'f' is

$$\bar{\bar{\tau}}_{t,f} = -\frac{2}{3}(\rho_f k_f + \mu_{t,f}\nabla\vec{v}_f)\bar{\bar{I}} + \mu_{t,f}(\nabla\vec{v}_f + \nabla\vec{v}_f{}^{tr}) \tag{26}$$

where, $\mu_{t,f}$ is the turbulent viscosity given by:

$$\mu_{t,f} = \rho_f C_\mu \frac{k_f^2}{\varepsilon_f} \text{ with } C_\mu\text{=0.09} \tag{27}$$

For the prediction of turbulent kinetic energy $k_f$ and its rate of dissipation $\varepsilon_f$, they are obtained from the following transport equations:

$$\nabla\cdot\left(\alpha_f\rho_f\vec{U}_f k_f\right) = \nabla\cdot\left(\alpha_f\frac{\mu_{t,f}}{\sigma_k}\nabla k_f\right) + \alpha_f G_{kf} - \alpha_f\rho_f\varepsilon_f + \alpha_f\rho_f\Pi_{kf} \tag{28}$$

$$\nabla\cdot\left(\alpha_f\rho_f\vec{U}_f k_f\right) = \nabla\cdot\left(\alpha_f\frac{\mu_{t,f}}{\sigma_\varepsilon}\nabla\varepsilon_f\right) + \alpha_f\frac{\varepsilon_f}{k_f}(C_{1\varepsilon}G_{k,f} - C_{1\varepsilon}\rho_f\varepsilon_f) + \alpha_f\rho_f\Pi_{\varepsilon f} \tag{29}$$

where $\Pi_{kf}$ and $\Pi_{\varepsilon f}$ represents the influence of the solid phase 's' on the fluid phase 'f' given by

$$\Pi_{kf} = \frac{k_{sf}}{\alpha_f\rho_f}(k_{sf} - 2k_f + \vec{v}_{sf.}\vec{v}_{dr}) \tag{30}$$

$$\Pi_{\varepsilon f} = C_{3\varepsilon}\frac{\varepsilon_f}{k_f}\Pi_{kf} \tag{31}$$

$\vec{v}_{dr}$ is the drift velocity given as:

$$\vec{v}_{dr} = \left(\frac{D_s}{\alpha_{sf}\alpha_s}\nabla\alpha_s - \frac{\mu_{t,f}}{\alpha_{sf}\alpha_s}\nabla\alpha_f\right) \tag{32}$$

$\nabla\alpha_s$ in above Eq. (32) takes into account the concentration fluctuations. $\vec{v}_{sf.}$ is the slip-velocity, the relative velocity between fluid phase and solid phase given by:

$$\vec{v}_{sf} = \vec{v}_s - \vec{v}_f \tag{33}$$

$D_s$ = eddy viscosity for solid section,

$\alpha_{sf}$ = constant (0.75),

$k_{sf}$ is the co-variance of the velocity of fluid phase and solid phase defined as the average of product of fluid and solid velocity fluctuations. $G_{k,f}$ is the production of the turbulent kinetic energy in the flow defined as the rate of kinetic energy removed from the mean and organized motions by the Reynolds stresses is given by:

$$G_{k,f} = \mu_{t,f}\left(\nabla\vec{v}_f + \nabla\vec{v}_f{}^t\right):\nabla\vec{v}_f \tag{34}$$

The constant parameters used in different equations are taken as:
$C_{1\varepsilon} = 1.44, C_{2\varepsilon} = 1.92, C_{3\varepsilon} = 1.2, \sigma_k = 1.0, \sigma_\varepsilon = 1.3.$

**2.3.3 Turbulence in the solid phase**

For the prediction of turbulence in solid phase, Tchen's theory (Lun et al. 1984) in homogeneous and steady turbulent flow for the dispersion of discrete particle is used. The representation of dispersion coefficients, turbulent kinetic energy and correlation functions of solid phase is based on the characteristics of continuous turbulent motion of fluid phase timescale and characteristics time.

$$\tau_{F,sf} = \alpha_s \rho_f K_{sf}^{-1} \left(\frac{\rho_s}{\rho_f} + C_{vm}\right) \tag{35}$$

The characteristics time of eddy particle interaction time:

$$\tau_{t,sf} = \tau_{t,f}\left[1 + C_\beta \xi^2\right]^{\frac{1}{2}} \tag{36}$$

$$\xi = \frac{|\vec{V}_r|}{\sqrt{\frac{2k_f}{3}}} \tag{37}$$

The characteristic time of energetic turbulent eddies:

$$\tau_{t,f} = \frac{3}{2} C_\mu \frac{k_f}{\varepsilon_f} \tag{38}$$

$|\vec{V}_r| = \vec{v}_{sf} - \vec{v}_{dr}$ , $|\vec{V}_r|$ being the average value of the local relative velocity between fluid and particle defined as slip and drift velocity.

$$C_\beta = 1.8 - 1.35cos^2\theta \tag{39}$$

$\theta$ is the angle between the mean particle velocity and mean relative velocity and $\eta_{sf}$ being the ratio between the two characteristic time given as:

$$\eta_{sf} = \frac{\tau_{t,sf}}{\tau_{F,sf}} \tag{40}$$

Turbulent kinetic energy of the solid phase, $k_s = k_f \left(\frac{b^2+\eta_{sf}}{1+\eta_{sf}}\right)$ (41)

Eddy viscosity for the solid phase, $D_s = D_{t,sf} + \left(\frac{2}{3}k_s - b\frac{1}{3}k_{sf}\right)\tau_{F,sf}$ (42)

Binary turbulent diffusion coefficient, $D_{t,sf} = \frac{1}{3}k_s \tau_{t,sf}$ (43)

where, b= (1+$C_{Vm}$) $\left(\frac{\rho_s}{\rho_f} + C_{Vm}\right)^{-1}$

**2.3.4 Transport equation for granular temperature $\Theta_s$**

The kinetic energy of random motion of solid particles is described by the granular temperature for the solid phase. The transport equation taken by the kinetic theory (Gidaspow et al. 1992) is in the following form:

$$\frac{2}{3}\nabla \cdot (\alpha_s \rho_s \vec{v}_s \Theta_s) = \left(-P_s \bar{\bar{I}} + \bar{\bar{\tau}}s\right) : \nabla \vec{v}_s + \nabla \cdot \left(k_{\Theta_s} \nabla \Theta_s\right) - \gamma_{\Theta_s} + \varphi_s \tag{44}$$

Here, the generation of energy by the solid stress tensor is defined by $\left(-P_s\bar{\bar{I}} + \bar{\bar{\tau}}s\right)$: $\nabla\vec{v}_s$. $k_{\Theta_s}$ being the diffusion coefficient given as:

$$k_{\Theta_s} = \frac{15\ {}_s\rho_s\alpha_s\sqrt{\Theta_s\pi}}{4(41-33\eta)}\left[1 + \frac{12}{5}\eta^2(4\eta-3)\alpha_s g_{0,ss} + \frac{16}{15\pi}(41-33\eta)\eta\alpha_s g_{0,ss}\right] \quad (45)$$

$k_{\Theta_s}\nabla\Theta_s$ is diffusive flux of granular energy.

$$\eta = \frac{1}{2}(1 + e_{ss}) \quad (46)$$

Collisional dissipation energy,

$$\gamma_{\Theta_s} = \frac{12(1-{e_{ss}}^2)g_{0,ss}}{d_s\sqrt{\pi}}\rho_s{\alpha_s}^2{\Theta_s}^{\frac{3}{2}} \quad (47)$$

$\varphi_{fs}$ is transfer of kinetic energy due to a random fluctuation in the particle's velocity from solid phase to fluid phase and is given by:

$$\varphi_{fs} = -3K_{fs}\Theta_s \quad (48)$$

### 2.3.5 Mesh

Meshing is an important part of the numerical modelling. Multi-zone meshing with the element order size 3 x $10^{-3}$m and skewness of 0.90 was adopted. The mesh was found to be compatible with the turbulence model and resulted in repeatable converged results.

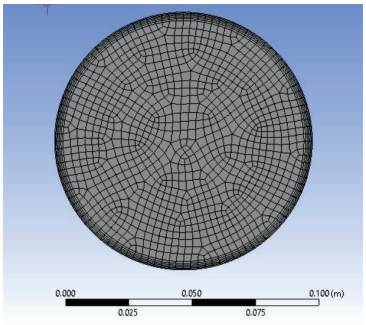


Figure 2: Mesh details of the pipeline in the cross-section

Figure 2 Shows the details of the meshing in the cross-sectional area of the pipeline. Inflation layers have been given to resolve the boundary layer better and to capture the gradient on walls efficiently.

Table 1

Details about the numerical setup

| | |
|---|---|
| Turbulence model | K- epsilon |
| Time step chosen | Steady state |
| Number of time step | Steady state |
| Volume fraction formulation | Implicit |
| Phase interaction | Water iron-ore: drag coefficient schiller-Nuamann |

Table 1 shows the details of the numerical scheme used in the study to simulate the flow of slurry through the pipeline.

## 3. RESULTS AND DISCUSSIONS

Figure 3 shows a comparative analysis between the pressure drop finding from the pipe-loop testing method (experimental) and the theoretical methods for different velocities. Initially, for lower velocity, the pressure loss comes almost equal from both experimental and theoretical method Chhabra and Richardson (2011). As the velocity increases, there is a significant difference between the theoretical pressure drop and the experimental data for pressure drop. The theoretical pressure drop obtained by Darby and Melson method is overpredicting and lies nowhere close to the experimental findings. Although the empirical equations are made with high precision taking account of major properties (such as absolute viscosity and yield stress for the given data set) but the losses occurring in the slurry pipeline operation possibly creates a huge gap between the actual pressure drop and the calculated pressure drop by the major methods and formulas available in the literature.

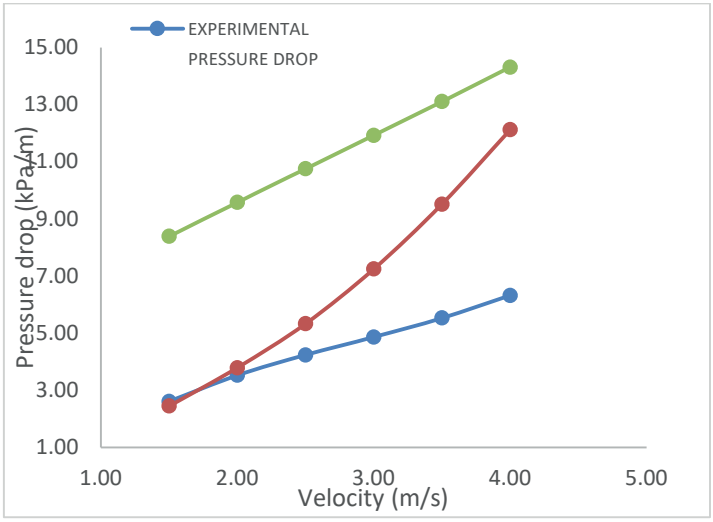


Figure 3 Experimental and theoretical pressure drop (based on methods available in literature) vs flow velocity plot at a concentration of 72% by weight (32.7% by volume)

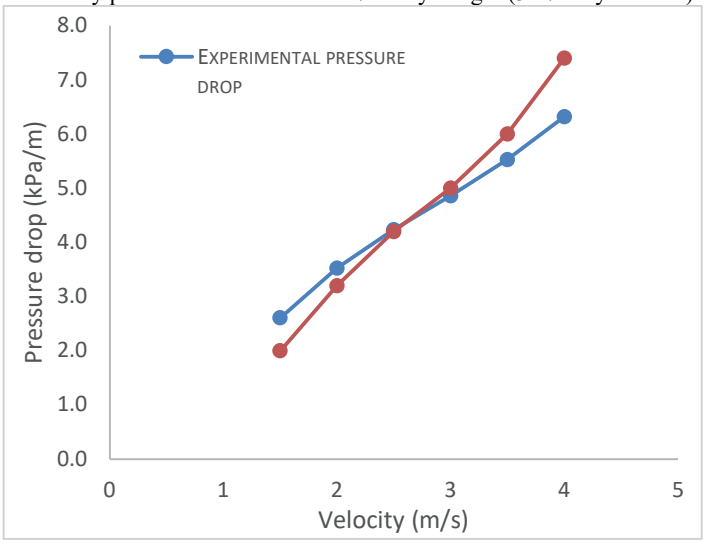


Figure 4 Experimental and numerical pressure drop (based on CFD modelling) vs velocity plot at a concentration of 72% by weight (32.7% by volume)

Figure 4 shows a comparative analysis between the experimental results and numerical results for pressure drop. Initially for the lesser velocity, the numerical results show some deviation from the experimental results but as the velocity increases, the results almost become equal in magnitude and further with increase in velocity it starts deviating again but with lesser degree of error.

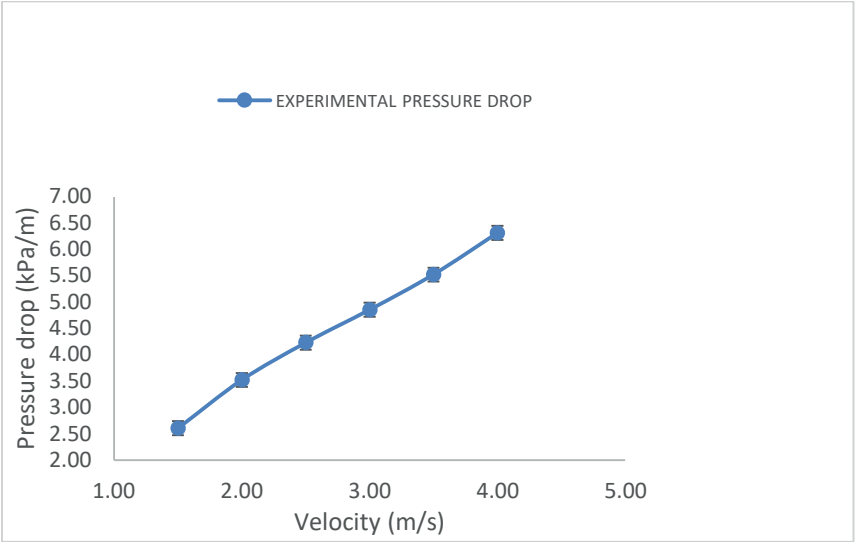


Figure 5: Experimental pressure drop vs velocity plot with error bars.

Figure 5 shows the pressure drop results found from the pipeloop test with corresponding error bars.

Table 2

Error values in theoretical and numerical pressure drops at different flow velocities for flow of iron ore slurry at a at a concentration of 72% by weight (32.7% by volume)

| S.no. | Velocity (m/s) | Error in theoretical results [Chhabra and Richardson] (%) | Error in theoretical results [Darby and Melson] (%) | Error in numerical results (%) |
|---|---|---|---|---|
| 1 | 1.5 | 6.06 | 221.59 | 23.3 |
| 2 | 2 | 7.42 | 171.63 | 9.2 |
| 3 | 2.5 | 25.78 | 153.94 | 0.8 |
| 4 | 3 | 49.05 | 145.37 | 2.9 |
| 5 | 3.5 | 72.1 | 137.07 | 8.5 |
| 6 | 4 | 91.8 | 126.47 | 17.11 |

Table 2 shows the error in theoretical and numerical results w.r.t. the pipe loop (experimental) pressure drops results. For theoretical pressure drop by Chhabra and Richardson, the error percentage keeps on increasing with the increase in velocity and reaches up to 91.8% for the theoretical pressure drop and for the theoretical pressure drop by Darby and Melson method, the error begins from 221% and reaches 126% for velocity of 4 m/s. Whereas in the CFD results, we can see the maximum error is 23.3% for the

lowest velocity. For the velocity of 2.5m/s the error in numerical results is just 0.8%, which shows how accurately CFD is predicting the pressure drop for iron ore slurry for the given data set.

The contours of different flow variable of iron ore slurry in a pipe can be affected by various factors, including the slurry's velocity, density, viscosity, and the pipe's geometry and surface roughness. Understanding these contours is essential for optimizing the transportation of iron ore slurry through pipelines. When iron ore slurry flows through a pipe, it tends to exhibit a specific flow profile.

The velocity profile with 0 velocity at the walls and increasing towards the centre are obtained for each case. Figure 6 shows the velocity profile for iron ore particles at the mid-length cross-section of the pipe for different velocities taken in the study. For the specified solid concentration, it has been discovered that the solids move at their fastest rate at the pipeline's centre in all velocity ranges. Furthermore, at all mean flow velocities shown, the velocity contours are symmetric about the pipeline's centre. The symmetry of the velocity contours is caused by the fact that when velocity and solid concentration rise, the momentum exchange between the solid particles also rises. This interaction between solids and solid walls generates turbulence in the pipeline slurry flow. As a result, solid particles in the middle of the pipe exhibit the highest velocity, while solid particulates close to the pipe wall exhibit lower velocity as a result of the viscous effect.

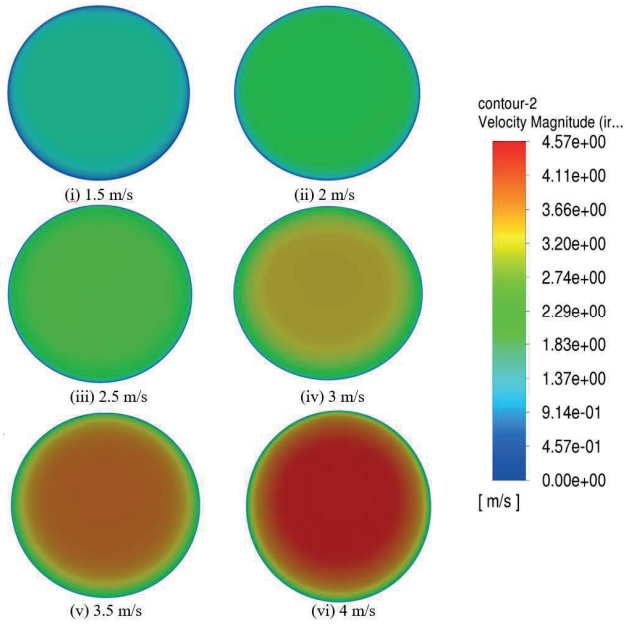


Figure 6 Velocity contours of iron ore particles at a concentration of 72% by weight (32.7% by volume) at different flow velocities

## 4. CONCLUSIONS

This study explored the potential of computational fluid dynamics (CFD) and theoretical methods to predict the pressure drop in the iron ore slurry pipeline. Comparisons were made with measurements taken from pipe loop test conducted in the laboratory of IIT Delhi. The velocity range was taken as 1.5m/s-4m/s. In the theoretical analysis, for with increasing velocity, the inaccuracy percentage w.r.t. the experimental results keep rising until it reaches 91.8% for 4m/s of velocity for Chhabra and Richardson method and maximum error of 221% for 1.5 m/s was found for Darby and Melson method. In contrast, the CFD results show that for lower velocities, the highest inaccuracy is 23.3%. The numerical findings' error for a velocity of 2.5 m/s are only 0.8%. This was a first attempt to predict such flows, and further tests are needed to confirm initial results.

## REFERENCES


1. Avksentiev, S. Y., & Makharatkin, P. N. (2017). Influence of rheology on pressure losses in hydrotransport system of iron ore tailings. Journal of Industrial Pollution Control, 33(1), 741-748.
2. Chhabra, R. P., & Richardson, J. F. (2011). Non-Newtonian flow and applied rheology: engineering applications. Butterworth-Heinemann.
3. D. R. Kaushal, T. Thinglas, Y. Tomita, S. Kuchii, and H. Tsukamoto, "CFD modeling for pipeline flow of fine particles at high concentration," Int. J. Multiph. Flow, vol. 43, pp. 85–100, 2012, doi: 10.1016/j.ijmultiphaseflow.2012.03.005.
4. D. Wu, B. Yang, and Y. Liu, "Pressure drop in loop pipe flow of fresh cemented coal gangue-fly ash slurry: Experiment and simulation," Adv. Powder Technol., vol. 26, no. 3, pp. 920–927, 2015, doi: 10.1016/j.apt.2015.03.009.
5. Darby, R., & Melson, J. (1981). How to predict the friction factor for flow of Bingham plastics.
6. Das, S. N., Biswal, S. K., & Mohapatra, R. K. (2020). Recent advances on stabilization and rheological behaviour of iron ore slurry for economic pipeline transportation. Materials Today: Proceedings, 33, 5093-5097.
7. Gidaspow, D., Bezburuah, R., Ding, J., 1992. Hydrodynamics of circulating fluidized beds, kinetic theory approach in fluidization VII. In: Proceedings of the 7th Engineering Foundation Conference on Fluidization.
8. Kaushal, D. R., Thinglas, T., Tomita, Y., Kuchii, S., & Tsukamoto, H. (2012). CFD modeling for pipeline flow of fine particles at high concentration. International Journal of Multiphase Flow, 43, 85-100.
9. Kumar N., Kaushal, D. R., Dwivedi, V. K., Singh, D. B., Sharma, S. K., & Yadav, J. K. (2020). CFD modeling of fly-ash slurry to analyse the concentration and velocity profiles. Materials Today: Proceedings, 21, 1695-1699.
10. Kumar N., Gopaliya, M.K. and Kaushal, D.R. (2019), Experimental investigations and CFD modeling for flow of highly concentrated iron ore slurry through horizontal pipeline, Particulate Science and Technology, An International Journal, Taylor and Francis Publications, Vol.37, No.2, pp, 232-250.
11. Lahiri, S. K., & Ghanta, K. C. (2009). Computational fluid dynamics simulation of solid-liquid slurry flow. Hydrocarbon processing (International ed.), 88(4), 99-104.
12. Lun, C.K.K., Savage, S.B., Jeffrey, D.J., Chepurniy, N., 1984. Kinetic theories for granular flow: inelastic particles in couette flow and slightly inelastic particles in a general flow field. J. Fluid Mech. 140, 223–256.
13. M. Tran, Z. Memon, A. Saieed, W. Pao, and F. Hashim, "Numerical simulation of two-phase separation in T-junction with experimental validation," J. Mech. Eng. Sci., vol. 12, no. 4, pp.

4216–4230, 2018, doi: 10.15282/jmes.12.4.2018.17.0363.
14. Matousek V., “Pressure drops and flow patterns in sand-mixture pipes,” Exp. Therm. Fluid Sci., vol. 26, no. 6–7, pp. 693–702, 2002, doi: 10.1016/S0894-1777(02)00176-0.
15. Messa, G. V., Yang, Q., Adedeji, O. E., Chára, Z., Duarte, C. A. R., Matoušek, V., ... & de Souza, F. J. (2021). Computational fluid dynamics modelling of liquid–solid slurry flows in pipelines: State-of-the-art and future perspectives. Processes, 9(9), 1566.
16. Mishra, S. S., & Sahoo, S. D. CFD Analysis of Pressure Variation inside Iron-Ore Slurry Pipelines.
17. Nagar H., Gupta, T., & Kumar, N. (2022). CFD modeling for the flow of fly ash slurry in straight pipeline. Materials Today: Proceedings, 57, 2223-2227.
18. Tarodiya, R., Khullar, S., & Gandhi, B. K. (2020). CFD modeling of multi-sized particulate slurry flow through pipe bend. Journal of Applied Fluid Mechanics, 13(4), 1311-1321.
19. Verma, O. P., Kumar, A., & Sikarwar, B. S. (2020). Numerical simulation and comparative analysis of pressure drop estimation in horizontal and vertical slurry pipeline. Journal of Mechanical Engineering and Sciences, 14(2), 6610-6624.
20. Yang, Y., Wang, H., Klein, B., & Wu, A. (2020). Shear-dependent yield stress of iron ore fine tailings in two-step flocculation process. Advances in Materials Science and Engineering, 2020, 1-12.